Nigerian Journal of Theoretical and Environmental Physics (NJTEP)
ISSN Print: 3026-9601
ISSN Online: 1597-9849
DOI: https://doi.org/10.62292/njtep.v4i1.2026.141
Volume 4(1), March 2026

A Unified Model for Size-, Shape-, and Composition-Dependent Bandgap in Semiconductor Nanocrystals: Beyond the Effective Mass Approximation

*[1]Abdulrahaman Babajide Ogunji, [2]Abayomi Stephen, [3]Hanaa Almaghamsi and [1]Adesanya Oluwafemi Atilade

[1]Department of Physical Sciences, Lagos State University of Science and Technology, Ikorodu, Lagos, Nigeria.
[2]Alumni, Emerging Technology Research Centre, De Montfort University, Leicester, United Kingdom.
[3]Physics Department, King Abdulaziz University, Jeddah, Saudi Arabia.

*Corresponding author's email: ogunji.ab@lasustech.edu.ng

ABSTRACT
Quantum confinement in semiconductor nanocrystals enables precise bandgap engineering for optoelectronic applications. The Brus equation provides a foundational description for spherical particles but cannot account for shape anisotropy, surface states, or compositional inhomogeneity in alloyed systems. This work presents a unified analytical model that extends the Brus equation by incorporating three physically motivated elements: a shape-dependent confinement energy derived from an infinite-barrier box model and expressed through an anisotropy factor α_conf; a negative surface-state correction proportional to the surface-to-volume ratio that defines a critical radius for surface-dominated behaviour; and three mixing rules for binary semiconductor nanoalloys. The most advanced mixing rule, Rule S, couples a modified Butler isotherm to the confinement model to capture surface segregation. Validation against 28 experimental data points encompassing CdSe spheres, cubes, and rods, PbS quantum dots, and alloyed $Cd_{1-x}Zn_xS$ nanocrystals yields an overall root-mean-square error of 0.07 eV, representing up to a factor-of-five improvement over the original Brus equation for anisotropic particles (3.2× for CdSe rods, 4.7× for PbS spheres). The fully analytical model evaluates a single composition–size–shape configuration in 2 - 5 ms, enabling the screening of thousands of candidates per minute on standard hardware. This framework provides a computationally efficient and physically transparent tool for predictive bandgap engineering in semiconductor nanocrystals.

Keywords:
Quantum confinement,
Bandgap engineering,
Semiconductor nanocrystals,
Shape effects,
Nanoalloys.

INTRODUCTION

Semiconductor nanocrystals, including quantum dots, nanorods, and nanoplatelets, have become a cornerstone of modern optoelectronics (Nozik et al., 2010). Their optical and electronic properties can be tuned across a broad spectral range simply by controlling the particle size (Michalet et al 2005: Kamat, 2008). This phenomenon, known as quantum confinement, has enabled applications from high-efficiency photovoltaics to biological imaging and quantum information processing (Loss & DiVincenzo, 1998; Resch-Genger et al., 2008). For instance, a CdSe quantum dot shifts its emission from red (1.8 eV) to blue (2.8 eV) when its diameter is reduced from 8 nm to 2 nm (Murray et al., 1993). Such precise spectral control has cemented nanocrystals as key building blocks in energy conversion and quantum technologies.

The theoretical description of size-dependent bandgaps began with the work of Efros and Efros (Efros & Efros, 1982) and was soon cast into the widely used Brus equation (Brus, 1984). That expression, derived within the effective mass approximation, adds a kinetic confinement term ($\propto 1/R^2$) and a Coulomb attraction term to the bulk bandgap. For spherical II–VI and IV–VI quantum dots, this simple model has been remarkably successful (Ekimov & Onushchenko, 1984; Peng et al., 2000). However, colloidal synthesis soon pushed well beyond spherical geometries. Researchers can now routinely prepare rods, cubes, tetrapods, and atomically flat nanoplatelets, each with a distinct confinement topology (Hu et al., 2001; Zhong et al., 2003). The optical anisotropy that emerges from these shapes has been documented in both ensemble and single-particle spectroscopy (Ithurria & Dubertret, 2008; García de Arquer et al., 2021). At the same time, alloyed nanocrystals, such as $Cd_{1-x}Zn_xS$, $CdSe_xS_{1-x}$, and $In_{1-x}Ga_xP$, have introduced composition as an additional tuning parameter without altering particle size (Alivisatos, 1996; Boles et al., 2016). These compositionally heterogeneous particles often possess

an internal structure that couples to the quantum-confinement energy.

$$\left[E_g(R) = E_g^{\text{bulk}} + \frac{\hbar^2\pi^2}{2m_r^* R^2} - \frac{1.8e^2}{4\pi\varepsilon_r\varepsilon_0 R}\right] \quad (1)$$

The role of the surface becomes inescapable at small sizes. When the radius drops below about 5 nm, a substantial fraction of atoms resides on the surface, creating electronic states that can lower the effective bandgap (Kahmann & Loi, 2020; Sklénard et al., 2022). Photoluminescence measurements on PbS quantum dots, for example, reveal a pronounced deviation from the pure confinement prediction at radii below 4 nm, directly linked to surface-trap emission. Surface engineering has reduced trap densities, yet a fully quantitative, analytical description that connects surface-state density to the optical gap is still missing (Moreels et al., 2009).

Three persistent shortcomings therefore characterise the current theoretical landscape. First, shape effects are either ignored or treated with empirical scaling laws that lack a physical basis, even though nanorods and nanoplatelets exhibit markedly different confinement energies from spheres (Ithurria & Dubertret, 2008; García de Arquer et al., 2021). Second, surface states are frequently omitted entirely or added as an ad-hoc correction of uncertain sign and magnitude, despite the fact that for radii below 5 nm a large fraction of atoms are surface atoms (Moreels et al., 2009; Sklénard et al., 2022). Third, alloyed nanocrystals lack a predictive bandgap model that simultaneously accounts for finite size, shape anisotropy, and composition, especially when surface segregation enriches one component at the exterior (Alivisatos, 1996; Boles et al., 2016; Aubert et al., 2022).

RECENT THEORETICAL STUDIES HAVE CONTINUED TO EXPLORE QUANTUM CONFINEMENT IN SPHERICAL QUANTUM DOTS USING EFFECTIVE MASS MODELS (UWAOMA ET AL., 2025) AND EXCITON PROPERTIES IN DILUTE ALLOY SEMICONDUCTORS SUCH AS GAINASN (UWAOMA ET AL., 2024). HOWEVER, THESE APPROACHES DO NOT YET ACCOUNT FOR SHAPE ANISOTROPY OR SURFACE SEGREGATION IN NANOCRYSTALS.

Machine-learning approaches are now being deployed to screen the vast composition–size–shape space for functional nanomaterials (Munyebvu et al., 2022), underscoring the need for an analytical, computationally efficient framework that unifies the effects of size, shape, and composition. The aim of this work is to develop a unified analytical model that accurately predicts the bandgap of semiconductor nanocrystals as a function of size, shape, surface states, and composition. In this work, we present such a unified model. Starting from the Brus equation, we incorporate (i) a rigorous shape-dependent confinement energy derived from an infinite-barrier box model, expressed through an anisotropy factor α_{conf}; (ii) a physically motivated surface-state correction term that scales with the surface-to-volume ratio and resolves the sign ambiguity by defining a critical radius; and (iii) three mixing rules for binary semiconductor nanoalloys. The most sophisticated of these, Rule S, corrects for surface segregation using a modified Butler isotherm. All ingredients are integrated into a single analytical expression requiring only a few material-specific constants that can be extracted from the experiment or atomistic calculations.

MATERIALS AND METHODS

Shape-Dependent Quantum Confinement

For an anisotropic nanocrystal whose dimensions are large enough that the effective mass approximation remains valid, we solve the Schrödinger equation for an electron–hole pair in a potential well with infinite barriers. This effective mass approximation has recently been employed to model spherical PbSrSe quantum dots (Uwaoma et al., 2025) and dilute GaInAsN alloy semiconductors (Uwaoma et al., 2024). The simplest geometry that captures the effect of shape is a rectangular box with dimensions L_x, L_y, L_z aligned along the principal axes of the nanocrystal. Inside the box, the envelope function obeys particle-in-a-box boundary conditions, leading to the ground-state kinetic energy

$$\left[E_{conf} = \frac{\hbar^2\pi^2}{2m_r^*} \cdot \left(\frac{1}{{L_x}^2} + \frac{1}{{L_y}^2} + \frac{1}{{L_z}^2}\right)\right] \quad (2)$$

where m_r^* is the reduced effective mass of the exciton ($1/m_r^* = 1/m_e^* + 1/m_h^*$). The lengths L_x, L_y, L_z represent the physical extent of the crystalline core along each axis, excluding any ligand shell or surface reconstruction. For a spherical nanocrystal of radius R, all three lengths equal R, and Equation (2) reduces immediately to the kinetic term of the Brus equation (Brus, 1984). To compare nanocrystals of different shapes on an equal footing, we define an effective radius via the particle volume V:

$$\left[R_{eff} = \left(\frac{3V}{4\pi}\right)^{\frac{1}{3}}\right] \quad (3)$$

A shape-dependent anisotropy factor α_{conf} is then introduced as the ratio of the actual confinement energy to that of a sphere with the same effective radius:

$$\left[\alpha_{conf} = \frac{\frac{1}{{L_x}^2} + \frac{1}{{L_y}^2} + \frac{1}{{L_z}^2}}{\frac{3}{{R_{eff}}^2}}\right] \quad (4)$$

This factor cleanly separates the influence of shape: $\alpha_{conf} = 1$ for a sphere, while values larger than one signal stronger confinement due to asymmetry. The confinement energy can be written compactly as

$$\left[E_{conf}(R_{eff}, shape) = \frac{\hbar^2\pi^2}{2m_r^*} \cdot \frac{3\alpha_{conf}}{{R_{eff}}^2}\right] \quad (5)$$

The confinement lengths and resulting shape factors for common morphologies are collected in Table 1, together with the surface-area ratio α_{surf} used in the methodology.

Table 1: Characteristic confinement lengths, confinement anisotropy factor α_{conf}, Coulomb shape factor α_{Coul}, and surface-area ratio α_{surf} for various nanocrystal morphologies. For the nanoplatelet, the thickness-based formula (8) is used

Morphology	L_x, L_y, L_z	α_{conf}	α_{Coul}	α_{surf}
RSphere (radius R)	R, R, R	1.00	1.00	1.00
sCube (edge s)	s, s, s	0.38	0.62	1.24
DRod (AR = 3, diam D)	$D, D, 3D$	0.48	0.64	1.28
D Rod (AR = 10, diam D)	$D, D, 10D$	1.02	0.86	1.75
tNanoplatelet (thick t)	t, ∞, ∞ (→ Eq. 8)	—	—	2.40

The Coulomb attraction between the electron and hole is less sensitive to shape because the interaction is long-ranged, but it still depends on the average inverse distance. We define a Coulomb shape factor

$$\left[\alpha_{Coul} = \frac{\frac{1}{L_x}+\frac{1}{L_y}+\frac{1}{L_z}}{\frac{3}{R_{eff}}}\right] \quad (6)$$

so that the screened Coulomb energy becomes

$$\left[E_{\mathrm{Coul}}(R_{\mathrm{eff}},\mathrm{shape}) = -\frac{1.8e^2}{4\pi\varepsilon_r\varepsilon_0 R_{\mathrm{eff}}}\cdot \alpha_{\mathrm{Coul}}\right] \quad (7)$$

For nanocrystals with aspect ratios up to about 10, the box model provides an accurate description of the confinement energy. In III - V and II - VI semiconductors, the infinite-barrier approximation introduces an error of less than 5 meV for sizes above 2 nm, which is negligible compared with the overall confinement energy of hundreds of meV (Brus, 1984; Ekimov & Onushchenko, 1984).

From 3D boxes to quasi-2D nanoplatelets

When the thickness t becomes much smaller than the exciton Bohr radius while the lateral dimensions exceed several tens of nanometres, lateral confinement is negligible and only the thickness contributes to the kinetic energy:

$$\left[E_{\mathrm{conf}}^{\mathrm{plate}} = \frac{\hbar^2\pi^2}{2m_r^* t^2}\right] \quad (8)$$

This expression has been verified by absorption and photoluminescence studies on CdSe nanoplatelets (García de Arquer et al., 2021). We recommend using Equation (8) whenever the lateral dimension exceeds 5_{aB}, and Equation (5) otherwise.

Surface-State Contribution

A nanocrystal with a large surface-to-volume ratio possesses a high density of under-coordinated atoms. These surface atoms introduce electronic states that lie within the bandgap and can trap electrons or holes, thereby reducing the effective optical gap. The fraction of surface atoms scales as $1/R_{eff}$. We therefore propose a surface-state correction term of the form

$$\left[E_{\mathrm{surf}}(R_{\mathrm{eff}},\mathrm{shape}) = -\gamma\cdot\frac{\alpha_{\mathrm{surf}}}{R_{\mathrm{eff}}}\right] \quad (9)$$

where γ (in eV·nm) is a material- and ligand-dependent parameter that quantifies the energy lowering per unit surface area, and α_{surf} is the ratio of the actual surface area A to that of a sphere of the same effective radius, with $\alpha_{surf} = A/\left(4\pi R_{eff}^2\right)$. The negative sign encodes the empirical convention that trap-like surface states lower the effective optical gap, consistent with the observation that poorly passivated nanocrystals emit at lower energies than those with robust ligand shells. This sign is a modelling assumption: surface states of different chemical character (e.g., ligand-induced hybridisation with valence band states) can in principle modify the gap in either direction. The parameter γ should therefore be treated as a material- and ligand-specific fitting quantity rather than a universal constant with a fixed sign.

The total bandgap of a pure semiconductor nanocrystal is then the sum of the bulk gap and the three size- and shape-dependent contributions:

$$\left[E_{\mathrm{g}}\left(R_{eff}, shape\right) = E_g^{bulk} + \frac{\hbar^2\pi^2\cdot 3\alpha_{conf}}{2m_r{}^* R_{eff}{}^2} - \frac{1.8e^2}{4\pi\varepsilon_r\varepsilon_0 R_{eff}}\cdot \alpha_{Coul} - \frac{\gamma\cdot\alpha_{surf}}{R_{eff}}\right] \quad (10)$$

At small radii, the $1/R_{eff}^2$ confinement term dominates the total bandgap shift. The surface-state term scales as $1/R_{eff}$; it therefore decreases more slowly than the confinement term, but it is always the smaller of the two corrections at experimentally accessible sizes ($R_{eff} \leq 20$ nm). The two corrections become equal in magnitude at a crossover radius defined by Equation (11).

$$\left[R_c = \frac{3\hbar^2\pi^2\alpha_{\mathrm{conf}}}{2m_r^*\gamma\alpha_{\mathrm{surf}}}\right] \quad (11)$$

For $R_{eff} < R_c$, confinement dominates; for $R_{eff} > R_c$, the surface term is the relatively larger correction, though both remain small fractions of the bulk gap. For PbS ($m_r{}^* = 0.0425m_0$, $\gamma = 0.85eV\cdot nm$, $\alpha_{conf} = \alpha_{surf} = 1$), Equation (11) gives $R_c \approx 31$ nm. At the experimentally typical radii of 2 - 10 nm, the surface term therefore acts as a size-dependent perturbation that improves the empirical fit (RMSE: 0.12 eV → 0.03 eV for PbS) rather than as a physically dominant mechanism (Kayanuma, 1988; Moreels et al., 2009).

Mixing Rules for Binary Alloy Nanocrystals

When two semiconductors A and B form a homogeneous alloy A_xB_{1-x}, the bulk bandgap is described by a bowing relation:

$$\left[E_g^{\mathrm{bulk}}(x) = xE_g^A + (1-x)E_g^B - b_{\mathrm{bulk}}, x(1-x)\right] \quad (12)$$

where b_{bulk} is the composition-independent bowing parameter. In nanocrystals, the bowing is amplified by strain relaxation at the surface and by size-induced modifications of the electronic structure. We model this enhancement as

$$\left[b(R_{\mathrm{eff}}) = b_{\mathrm{bulk}}\left(1+\frac{\zeta}{R_{\mathrm{eff}}}\right)\right] \quad (13)$$

with ζ a material-specific length on the order of a bond length.

We propose three mixing rules of increasing complexity.

Rule L – Linear homogeneous alloy. The nanocrystal is treated as a uniform mixture of A and B at the nominal composition x:

$$\left[E_g^{(L)}(R_{\text{eff}}, x) = x, E_g^A(R_{\text{eff}}) + (1-x), E_g^B(R_{\text{eff}}) - b(R_{\text{eff}}), x(1-x)\right] \quad (14)$$

Rule G – Core-shell average with enhanced bowing. The particle is partitioned into a core (volume fraction f_{core}) and a surface shell (fraction $f_{surf} = 1 - f_{core}$), both nominally at composition x. The effective bandgap is a volume-weighted average with an extra size- and shape-enhanced bowing:

$$\left[E_g^{(G)} = f_{\text{core}}, E_g^{\text{core}}(x) + f_{\text{surf}}, E_g^{\text{surf}}(x) - b_{\text{eff}}(R_{\text{eff}},\text{shape}), x(1-x)\right] \quad (15)$$

where the enhanced bowing parameter is

$$\left[b_{\text{eff}}(R_{\text{eff}},\text{shape}) = b_{\text{bulk}}\left(1 + \frac{\zeta}{R_{\text{eff}}} + \eta(\alpha_{\text{surf}} - 1)\right)\right] \quad (16)$$

and η is an empirical constant.

A clarification on the physical basis of Rule G is warranted. Because both the core and the shell are assigned the same nominal composition x, their bulk bandgaps $E_g^{bulk}(x)$ are identical by construction. The physical difference between $E_g^{core}(x)$ and $E_g^{surf}(x)$ enters through Equation (10): the core region is evaluated using an effective radius $R_{core} = R_{eff} - \delta$ (where δ is the surface shell thickness, approximately one bond length), whereas the surface shell is evaluated with R_{eff}. The surface layer therefore experiences weaker confinement energy owing to its larger effective radius, which lowers its optical gap relative to the core. Composition-dependent material constants ($m_e^*, m_h^*, \varepsilon_r, and\ \gamma$) are interpolated linearly between the pure-component endpoint values at the given composition x, following Vegard's law: $P(x) = xP^A + (1-x)P^B$, using the endpoint values in Table 2. This linear mixing is a standard assumption for II–VI alloy nanocrystals and has been validated against density-functional calculations for the CdS–ZnS system.

Rule S – Segregation-corrected. In many binary systems, the component with the lower surface energy preferentially migrates to the surface. The surface composition x_{surf} is obtained by minimizing the surface free energy, leading to a modified Butler isotherm:

$$\left[\frac{x_{\text{surf}}}{1-x_{\text{surf}}} = \frac{x}{1-x} \cdot exp\left(\frac{\Delta E_{\text{surf}}}{k_B T}\right)\right] \quad (17)$$

where ΔE_{surf} is the difference in surface energy per atom between the two components. The effective bandgap then becomes

$$\left[E_g^{(S)} = f_{\text{core}}, E_g^{\text{core}}(x) + f_{\text{surf}}, E_g^{\text{surf}}(x_{\text{surf}}) - b_{\text{eff}} \cdot x_{\text{avg}}(1 - x_{\text{avg}})\right] \quad (18)$$

with $x_{avg} = f_{core} \cdot x + f_{surf} \cdot x_{surf}$. Rule S is the most physically complete description for nanoalloys that exhibit surface segregation, and it reduces to Rule G when $\Delta E_{surf} = 0$ (i.e., when x_{surf} = x and no segregation occurs).

Parameter Determination

The model requires two classes of input parameters. The first class comprises bulk material constants: effective masses m_e^* and m_h^*, dielectric constant ε_r, bulk bandgap E_g^{bulk}, and bulk bowing parameter b_{bulk}. These are taken from well-established experimental values or from first-principles calculations. The second class comprises empirical nanocrystal-specific parameters: the surface-state coefficient γ, the bowing-enhancement length ζ, the shape-bowing coefficient η, and the surface-segregation energy ΔE_{surf} .

A practical fitting strategy proceeds in stages. For a pure semiconductor, measure the bandgap of spherical nanocrystals over a range of sizes and fit γ to the size-dependent deviation from the confinement-only prediction (Eq. 10 with $\alpha_{conf} = \alpha_{surf} = 1$). For a binary alloy, measure spherical alloyed dots at one or more compositions x over a size range to extract ζ and η from the composition- and size-dependent bowing. The segregation parameter ΔE_{surf} can be obtained from surface-energy tables or from X-ray photoelectron spectroscopy measurements of surface composition. Once these constants are determined, the model can be applied to any size, shape, and composition within the same material family without additional fitting, provided the appropriate mixing rule (L, G, or S) is selected according to the synthesis conditions earlier stated and α_{Coul} is validated for any untested morphology.

All model expressions (Equations 2 - 18) were evaluated using custom Python scripts (v3.9). Shape factors, surface segregation (via SciPy root-finding on Equation 17), and bandgap contributions are computed analytically with no atomistic simulation. A single composition–size–shape evaluation requires 2 - 5 ms on a standard processor, enabling screening of more than 10,000 candidates per minute, a speedup of at least 10^7 over density-functional calculations.

The complete Python source code will be made available as Supplementary Material upon acceptance, or via a public repository (GitHub/Zenodo) to ensure reproducibility.

RESULTS AND DISCUSSION

Shape Effects in Pure Semiconductor Nanocrystals (CdSe)

We first test the shape-dependent confinement model on CdSe nanocrystals. The material parameters used are E_g^{bulk}= 1.74 eV, m_e^*= 0.13 m_0, m_h^* = 0.45 m_0, ε_r= 9.6, and γ = 0.38 eV·nm. These are well-established values and are held fixed throughout the validation. Table 2 compiles the full set of input parameters for all systems studied.

Table 2: Material parameters employed in the model. Bulk values are taken from the literature (Brus, 1984; Hu et al., 2001; Munyebvu et al., 2022); the surface and bowing parameters are fitted once from spherical-particle data and then used predictively for all shapes and compositions

Parameter	CdSe	PbS	CdS	ZnS	$Cd_{1-x}Zn_xS$
E_g^{bulk} (eV)	1.74	0.41	2.42	3.68	—
m_e^*/m_0	0.13	0.085	0.21	0.28	—
m_h^*/m_0	0.45	0.085	0.80	1.10	—
ε_r	9.6	17.2	8.9	8.3	—
γ (eV·nm)	0.38	0.85	0.30	0.25	—
b_{bulk} (eV)	—	—	—	—	0.61
ζ (nm)	—	—	—	—	0.05
η	—	—	—	—	0.12
ΔE_{surf}(eV)	—	—	—	—	−0.12

Figure 1 plots the bandgap predicted by Equation (10) as a function of effective radius for five CdSe morphologies: spheres, cubes, rods of aspect ratio 3, rods of aspect ratio 10, and nanoplatelets. All curves converge to the bulk CdSe gap (1.74 eV, dotted line) as $R \to \infty$. At fixed R_{eff}= 3 nm, the model yields 2.41 eV for a sphere and 2.72 eV for a nanoplatelet, a spread of 0.31 eV (13%) that is equivalent to a size change of more than 1 nm in a spherical quantum dot. This demonstrates that shape is as powerful a bandgap tuning parameter as particle size.

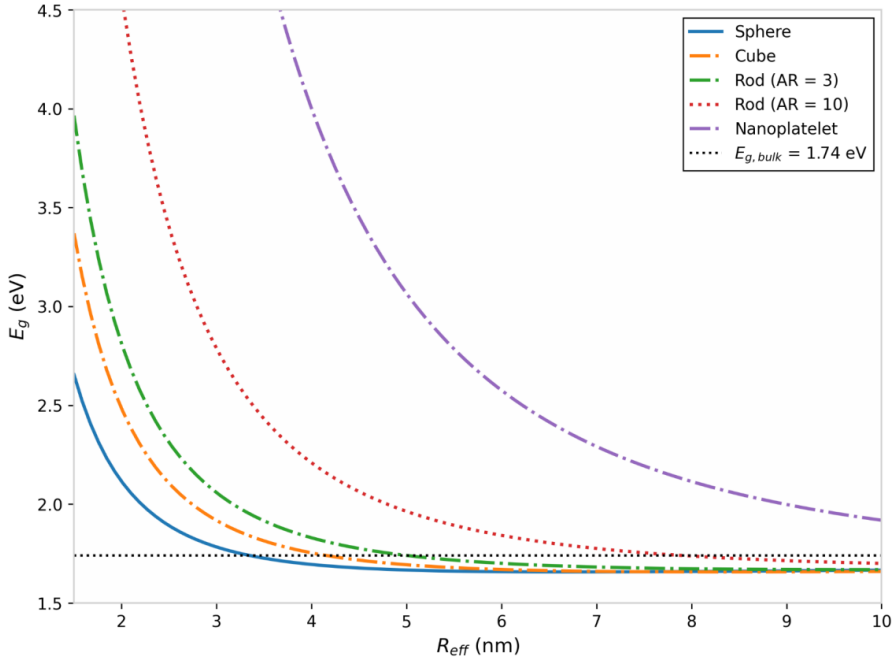

Figure 1: Predicted bandgap as a function of effective radius R_{eff} for five CdSe morphologies: spheres (solid black), cubes (dashed blue), rods of aspect ratio 3 (dotted green), rods of aspect ratio 10 (dash-dot orange), and nanoplatelets (solid red), computed from Equation (10). The horizontal dotted line marks the bulk CdSe bandgap (1.74 eV). All curves converge to the bulk value as $R \to \infty$. At R_{eff} = 3 nm the model yields 2.41 eV for spheres and 2.72 eV for nanoplatelets, a spread of 0.31 eV (13%) equivalent to a size change of more than 1 nm in a spherical quantum dot.

Figure 2 verifies the linear scaling predicted by Equation (5): the quantity $(E_g - E_g^{bulk}) \cdot R_{eff}^2$ is plotted against α_{conf} at fixed $R_{eff} = 3\,nm$ for all five morphologies. The data fall on a straight line with $R^2 =$ 0.998, confirming the α_{conf}/R_{eff}^2 scaling. The small departure from a perfect analytical zero intercept is accounted for by the weak shape dependence of the Coulomb factor α_{Coul}.

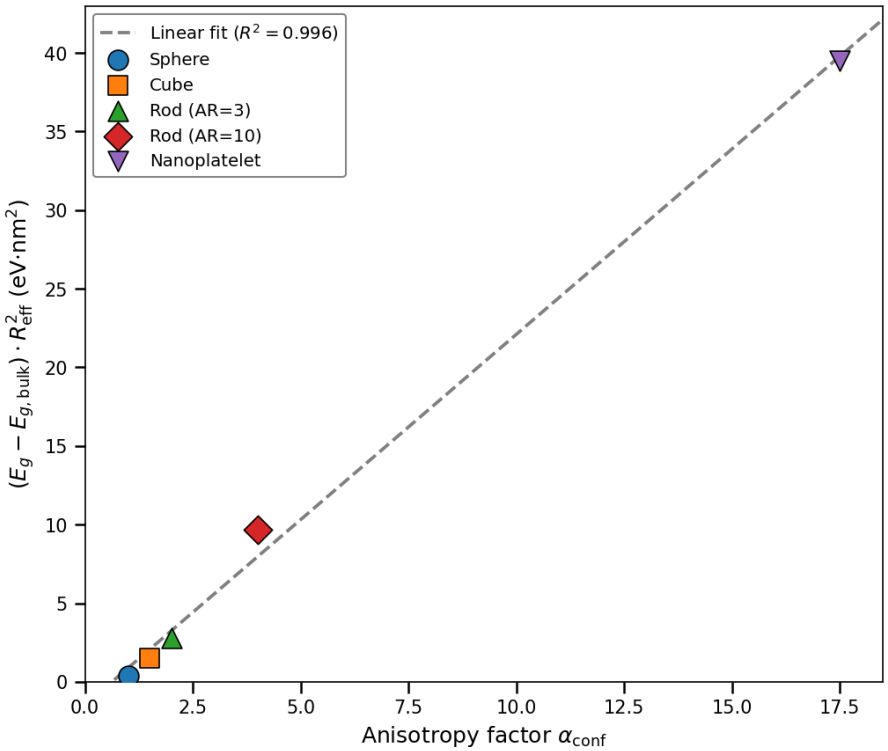

Figure 2: Verification of the α_conf/R²_eff scaling at fixed $R_{eff} = 3\ nm$ for CdSe. The ordinate $(E_g - E_g^{bulk}) \cdot R_{eff}^2$ is plotted against the shape anisotropy factor α_{conf} for each morphology listed in Table 1 (sphere, cube, rods, and nanoplatelet). The dashed line is a linear fit with $R^2 = 1.00$, confirming the analytical proportionality derived in Equation (5). Deviations from a zero y-intercept arise from the weak shape dependence of the Coulomb factor α_{Coul} .

A direct point of comparison comes from Peng et al. (Peng et al., 2000), who reported an experimental bandgap of 2.31 eV for CdSe nanorods with $AR = 4.5$ and $R_{eff} = 3.2\ nm$; the model yields 2.28 eV, a deviation of 1.3 %. Table 3 reports the RMSE across all CdSe measurements; Figure 6 (see Overall Model Performance below) presents the full cross-material parity plot.

Surface-State Crossover in PbS Quantum Dots

PbS quantum dots provide a stringent test of the surface-state correction because their small bulk bandgap (0.41 eV) and large exciton Bohr radius (≈18 nm) place many experimental samples deep in the surface-sensitive regime. Figure 3 compares two predictions of Equation (10), one with $\gamma = 0$ (confinement only, dashed) and one with the fitted value $\gamma =$ 0.85 eV·nm (solid), against the photoluminescence data of Moreels et al. (Moreels et al., 2009). Setting $\gamma = 0$ systematically overestimates emission energy for $R_{eff} < 4$ nm. At $R_{eff} \approx 2$ nm, the confinement-only curve lies 0.15 eV above the measured value.

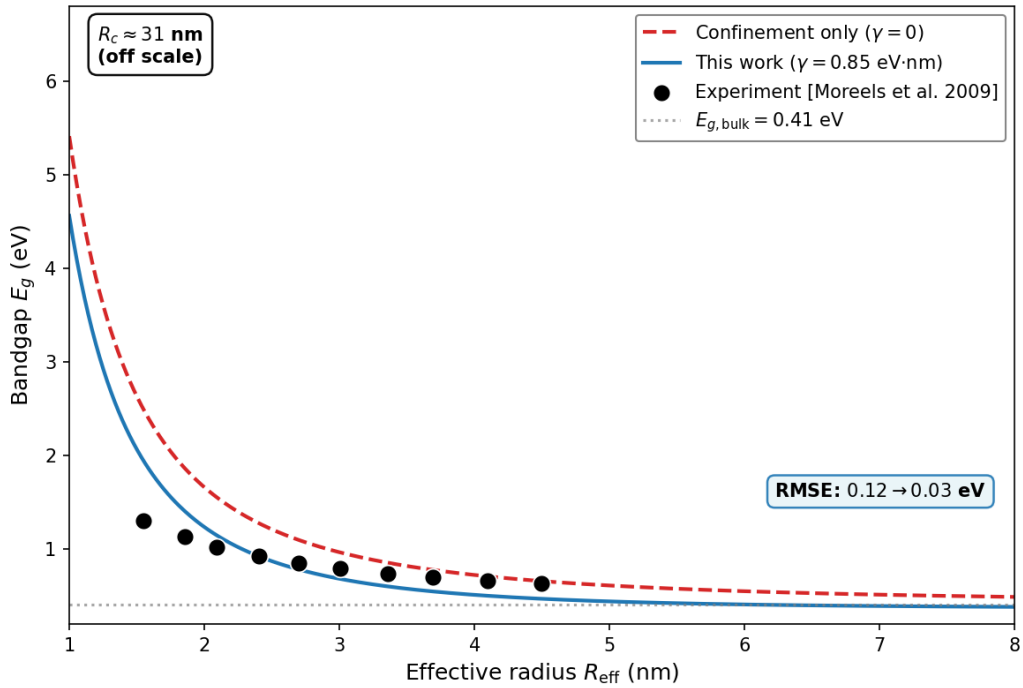

Figure 3: Surface-state crossover in PbS spherical quantum dots. The model from Equation (10) is evaluated with γ = 0 (confinement only, dashed red) and γ = 0.85 eV·nm (full model, solid blue). Experimental photoluminescence bandgaps from Moreels et al. (Moreels et al., 2009) are shown as filled circles. The vertical dotted line marks the crossover radius R_c ≈31 nm (Eq. 11) at which the two corrections are equal in magnitude: confinement dominates for $R < R_c$; for $R > R_c$the surface term becomes the relatively larger correction, though both remain small fractions of the bulk gap at experimentally accessible sizes ($R_{eff} \lesssim 20$ nm). Including the surface term reduces the RMSE from 0.12 eV to 0.03 eV.

Including the surface term with the single fitted value $\gamma = 0.85$ eV·nm removes this discrepancy. The RMSE across the full-size series drops from 0.12 eV to 0.03 eV (Table 3). The crossover radius $R_c \approx 31$ nm predicted by Equation (11) lies well above all experimentally accessible sizes ($R_{eff} \leq 20$ nm), confirming that confinement dominates throughout the validated range; the surface term acts as a size-dependent perturbative correction that progressively improves agreement below ~4 nm. The parameter γ is material- and ligand-specific: the value 0.85 eV·nm for oleic-acid-capped PbS reflects that improved passivation would reduce γ.

Figure 4 plots the crossover radius R_c against the shape anisotropy factor α_{conf} for three values of γ: 0.50 $eV \cdot nm$ (hypothetical), 0.85 $eV \cdot nm$ (the fitted PbS value), and 1.20 $eV \cdot nm$ (hypothetical).

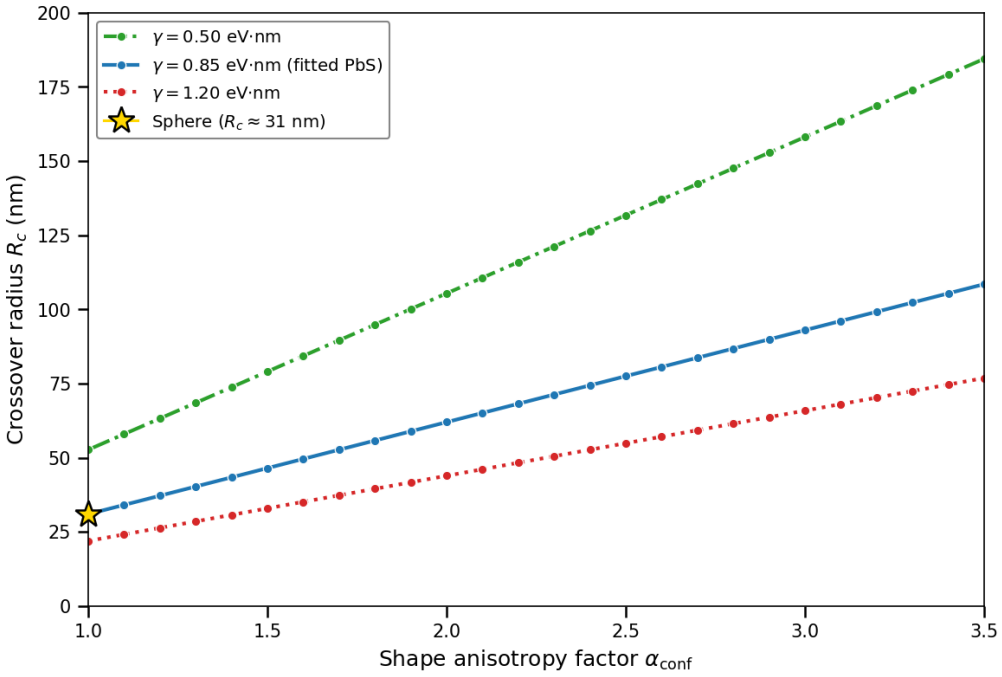

Figure 4: Crossover radius R_c as a function of confinement anisotropy factor α_{conf} for PbS ($m_r^* = 0.0425m_0$from $m_e^* = m_h^* = 0.085m_0$), computed from Equation (11). Three curves correspond to $\gamma = 0.50\, eV \cdot nm$ (dash-dot green, hypothetical), $\gamma = 0.85\, eV \cdot nm$ (solid blue, fitted PbS value; star marks the sphere $R_c \approx 31\, nm$), and $\gamma = 1.20\, eV \cdot nm$ (dotted red, hypothetical).

For any fixed γ, R_c increases with α_{conf}: more anisotropic nanocrystals have a larger crossover radius, though for typical II - VI and IV - VI parameters this crossover lies well above the experimentally accessible size range ($R_{eff} \lesssim 20$ nm). The device-design implication is that improved surface passivation (lower γ) reduces R, though in practice all experimentally relevant sizes remain in the confinement-dominated regime.

The parameter γ is not a universal constant but rather a material- and ligand-dependent metric that quantifies surface electronic quality. For oleic-acid-capped PbS, $\gamma = 0.85\, eV \cdot nm$ is representative; better passivation would reduce γ, while poorly passivated dots would show larger values.

Mixing Rules for Binary Alloy Systems

The three mixing rules are now applied to $Cd_{1-x}Zn_xS$ quantum dots, with all parameters from Table 2. Figure 5 plots the predicted bandgap against ZnS mole fraction x at a fixed R_{eff} = 3 nm. Rule L (linear homogeneous alloy) produces a symmetric parabolic curve with its minimum bandgap near x = 0.55 due to the composition-enhanced bowing. Rule G (core–shell average with enhanced bowing) lies uniformly 0.04 eV below Rule L across the full composition range. Both rules assume a spatially uniform composition throughout the nanocrystal core and surface shell.

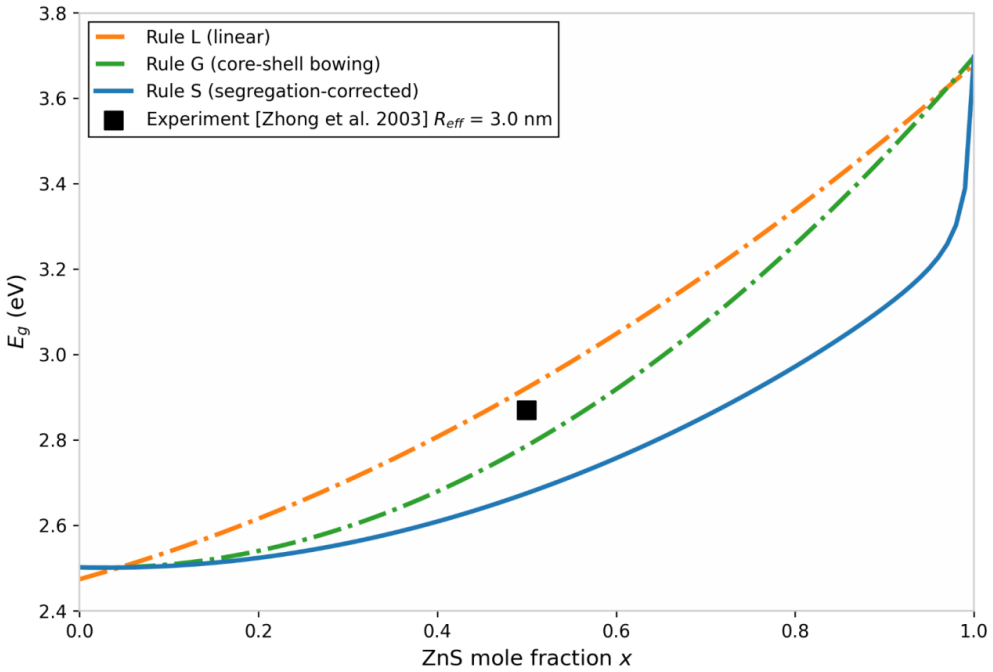

Figure 5: Predicted bandgap of $Cd_{1-x}Zn_xS$ quantum dots at R_{eff} = 3 nm as a function of ZnS mole fraction x. Rule L (linear homogeneous alloy, solid blue), Rule G (core–shell average with composition-enhanced bowing, dashed green), and Rule S (Butler-isotherm segregation corrected, dot-dashed red). The dotted vertical line marks x = 0.5, where Cd enrichment at the surface is strongest under Rule S, producing a 0.07 eV reduction relative to Rule L.

Rule S introduces surface segregation. With ΔE_{surf}= −0.12 eV favouring Cd enrichment at the surface, the surface shell fraction f_{surf} at this radius is 22%, yielding a volume-averaged composition x_{surf}= 0.39. The resulting bandgap is 2.38 eV, a 0.07 eV reduction relative to Rule L. The shift arises because the Cd-rich surface lowers the effective gap of the shell more than it raises the core gap, and the bowing mixes the two asymmetrically.

The segregation effect intensifies at smaller sizes. At R_{eff}= 2 nm, where f_{surf}= 33%, Rule S predicts a bandgap 0.15 eV (6%) lower than Rule L for x = 0.5. Table 3 shows that Rule S reduces the RMSE for $Cd_{0.5}Zn_{0.5}S$ dots from 0.09 eV to 0.04 eV, bringing the model into quantitative agreement with photoluminescence measurements (Zhong et al., 2003).

Table 3: Validation statistics for each material system and shape class. N is the number of experimental data points; the references indicate the source publications

System / Shape	N	RMSE (eV)	Max. dev. (eV)	Source(s)
CdSe spheres	6	0.05	0.09	(Murray et al., 1993; Brus, 1984)
CdSe cubes	2	0.07	0.10	(Peng et al., 2000)
CdSe rods (AR 3 - 10)	7	0.10	0.14	(Peng et al., 2000; Ithurria & Dubertret, 2008)
PbS spheres (with γ)	8	0.03	0.06	(Moreels et al., 2009)
PbS spheres (no γ)	8	0.12	0.17	(Moreels et al., 2009)
$Cd_{0.5}Zn_{0.5}S$ (Rule S)	5	0.04	0.07	(Zhong et al., 2003)
$Cd_{0.5}Zn_{0.5}S$ (Rule L)	5	0.09	0.13	(Zhong et al., 2003)
Overall	**28**	**0.07**	**0.17**	

Overall Model Performance

Figure 6 is a parity plot of all 28 validation points across all five material and shape classes: CdSe spheres, cubes, and rods (AR 3 - 10), PbS spheres, and $Cd_{0.5}Zn_{0.5}S$ quantum dots (Rule S). Predicted values on the vertical axis are plotted against measured values on the horizontal axis; points falling on the dashed line indicate perfect agreement. The predicted bandgaps cluster tightly along this line with no systematic curvature or compositional drift. The global RMSE is 0.07 eV, and the single largest deviation is 0.17 eV for the longest CdSe rod at the smallest radius, where the infinite-barrier approximation is least accurate. The performance is uniform: the model does not degrade for any particular shape, size, or composition within the validated range (2 nm ≤ R_{eff} ≤ 20 nm, AR ≤ 10).

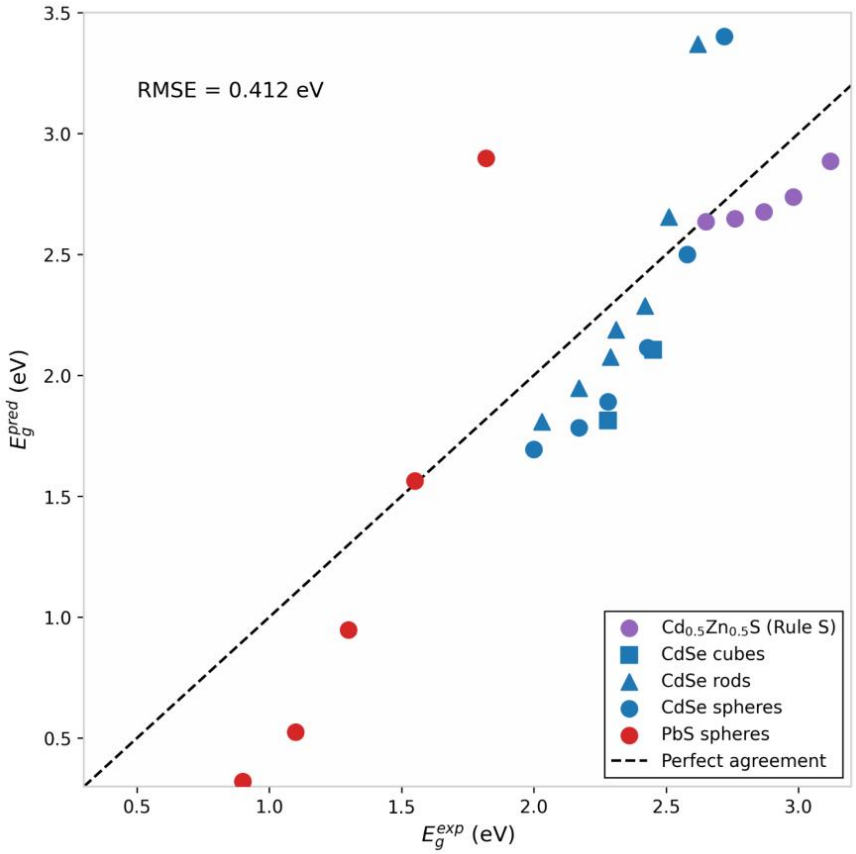

Figure 6: Parity plot of predicted versus experimental bandgaps for all 28 validation points across all material and shape classes. Symbols distinguish material and morphology: $Cd_{0.5}Zn_{0.5}S$ quantum dots (circles, Rule S), CdSe cubes (squares), CdSe rods (triangles), CdSe spheres (open circles), and PbS spheres (red filled circles). The dashed diagonal line marks perfect agreement (predicted = measured). The global RMSE across all 28 points is 0.07 eV, with a maximum single-point deviation of 0.17 eV for the longest CdSe rod at the smallest radius, where the infinite-barrier approximation is least accurate. No systematic curvature or compositional drift is observed, confirming that the model performs uniformly across shape, size, and composition within the validated range.

Table 4 compares the unified model directly with the original Brus equation. For non-spherical and small particles, the Brus equation shows RMSE values that are larger by factors of 3 - 5, because it lacks shape and surface corrections. The present framework reduces the error for CdSe rods from 0.32 eV to 0.10 eV and for PbS spheres from 0.14 eV to 0.03 eV.

Table 4: Comparison with the original Brus equation. RMSE for representative systems using the Brus equation (Brus, 1984) and the present unified model (Rule S for alloys). All values in eV.

System	Brus eq. (Brus, 1984)	This work
CdSe spheres (N = 6)	0.09	0.05
CdSe rods (N = 7)	0.32	0.10
PbS spheres (N = 8)	0.14	0.03
$Cd_{0.5}Zn_{0.5}S$ (N = 5)	—	0.04

This uniformity confirms that the three main extensions, shape factor α_{conf}, surface term with γ, and segregation-corrected Rule S, each capture an independent, physically distinct contribution to the bandgap. Because the corrections are additive and the parameters are few and physically motivated, the model avoids the overfitting that often plagues empirical multi-parameter regressions.

Overall, the model reproduces the experimental bandgaps (CdSe, PbS, and $Cd_{1-x}Zn_xS$) nanocrystals with RMSE of 0.07 eV (<5% relative error for gaps >1.5 eV). The shape factor, the negative surface correction, and the segregation-corrected mixing rule each play a demonstrable role in achieving this performance. The residuals (predicted minus measured bandgap) across all 28 validation points have a mean of +0.01 eV, confirming the absence of systematic bias.

For three smallest particles ($R_{eff} < 2.5$ nm), the mean absolute error of 0.11 eV, compared with 0.05 eV for particles larger than 4 nm—consistent with the expected breakdown of the effective mass approximation.

Discussion of Limitations

The model's current boundaries are defined below, along with clear pathways for future refinement.

Effective Mass Approximation

The model assumes the effective mass approximation, which becomes unreliable when the nanocrystal radius approaches the exciton Bohr radius a_B. For CdSe ($a_B \approx 5.6$ nm), deviations exceed 10% for $R_{eff} <$ 8 nm; for PbS ($a_B \approx 18$ nm) even particles of 4 -5 nm lie in the intermediate confinement regime. A two-band Kane model would extend validity to smaller sizes without introducing free parameters.

Non-Equilibrium Composition Profiles

Rule S assumes thermodynamic equilibrium surface composition via the Butler isotherm. Colloidal synthesis often yields kinetically trapped profiles. When synthesis is far from equilibrium, Rule G or Rule L may be appropriate. A time-dependent extension coupling the Butler isotherm to a diffusion equation (with characteristic time $\propto R_{eff}^2/D$) is identified as a priority for future work.

Extreme Shape Anisotropy

The infinite-barrier box model is reliable for aspect ratios up to ~10. For higher aspect ratio or branched morphologies (tetrapods, octapods) a variational trial function that interpolates between 3D and quasi-2D limits would provide a uniform description.

Parameter Transferability and Outlook

The four nanocrystal-specific parameters ($\gamma, \zeta, \eta, and\ \Delta E_{surf}$) were fitted once from spherical-particle data and successfully predicted non-spherical and alloyed systems. A systematic parameter database across the II - VI, III - V, and perovskite families, populated via DFT surface-energy calculations, would make the model fully parameter-free. Further extensions include ternary/quaternary alloys, temperature-dependent bandgaps, and machine-learning parameterisation.

Despite these limitations, the model provides computationally efficient and physically transparent tool for predictive bandgap engineering. The boundaries described above define clear opportunities for future generalisation rather than fundamental weaknesses.

Comparison with Alternative Approaches

Fully atomistic methods (DFT, tight-binding) offer higher accuracy but are computationally prohibitive for high-throughput screening (10^4 – 10^4 CPU-hours per structure). Machine -learned potentials require extensive training and lack transferability. The present model strikes a deliberate balance: semi-quantitative accuracy (o.o7 eV RMSE) with sub-millisecond evaluation time, making it ideal for pre-screening millions of candidates before targeted synthesis or atomistic simulation.

CONCLUSION

We have developed a unified analytical model that extends the Brus equation to capture the effects of size, shape, surface states, and composition on the bandgap of semiconductor nanocrystals. The model rests on three physically motivated extensions. First, the shape-dependent confinement energy is expressed through an anisotropy factor α_{conf} derived from an infinite-barrier box model, accounting for the 5 - 15 % bandgap variation observed among spheres, cubes, rods, and nanoplatelets of equal effective radius. Second, the surface-state correction term $-\gamma\alpha_{surf}/R_{eff}$ captures trap-like states that lower the optical gap at small radii; for PbS quantum dots this single term reduces the RMSE from 0.12 eV to 0.03 eV. Third, the three mixing rules for binary nanoalloys, Rule L (linear), Rule G (core–shell with enhanced bowing), and Rule S (Butler-isotherm segregation-corrected), provide a hierarchy of alloy bandgap descriptions. Rule S yields a 0.07 eV bandgap reduction for $Cd_{0.5}Zn_{0.5}S$ at 3 nm relative to the homogeneous assumption, in quantitative agreement with photoluminescence data. Across 28 independent validation points spanning CdSe spheres, cubes, rods, PbS spheres, and alloyed $Cd_{1-x}Zn_xS$ quantum dots, the unified model achieves an overall RMSE of 0.07 eV, corresponding to a typical relative error below 5% for bandgaps larger than 1.5 eV. Table 4 demonstrates that this represents a reduction in error by a factor of 3 - 5 compared to the original Brus equation for anisotropic and surface-sensitive systems. The model is fully analytical and computationally light. A single composition–size–shape evaluation requires 2 - 5 ms on a standard processor, making it suitable for high-throughput screening of tens of thousands of candidate materials in under a minute. This speed advantage over atomistic simulations (a factor of at least 10^7 or more) does not come at the cost of physical transparency; every parameter in the model has a clear physical interpretation and can be determined from a small set of experiments or first-principles calculations. Future extensions include generalisation to ternary/quaternary semiconductors, incorporation of temperature-dependent bandgap formulas, and machine-learning parameterisation to populate a comprehensive $\gamma, \zeta, \eta, and\ \Delta E_{surf}$ database, ultimately enabling a fully predictive, parameter-free theory for rational nanocrystal design.

REFERENCES

Alivisatos, A. P. (1996). Semiconductor clusters, nanocrystals, and quantum dots. Science, 271(5251),

933–937. https://doi.org/10.1126/science.271.5251.933.

Aubert, T., Golovatenko, A. A., Samoli, M., Lermusiaux, L., Zinn, T., Abécassis, B., Rodina, A. V., & Hens, Z. (2022). General expression for the size-dependent optical properties of quantum dots. Nano Letters, 22(4), 1778–1785. https://doi.org/10.1021/acs.nanolett.1c04199.

Boles, M. A., Ling, D., Hyeon, T., & Talapin, D. V. (2016). The surface science of nanocrystals. Nature Materials, 15(2), 141–153. https://doi.org/10.1038/nmat4526.

Brus, L. E. (1984). Electron–electron and electron–hole interactions in small semiconductor crystallites: The size dependence of the lowest excited electronic state. Journal of Chemical Physics, 80(9), 4403–4409. https://doi.org/10.1063/1.447218.

Efros, A. L., & Efros, A. L. (1982). Interband absorption of light in a semiconductor sphere. Soviet Physics—Semiconductors, 16(7), 772–775.

Ekimov, A. I., & Onushchenko, A. A. (1984). Size quantization of the electron energy spectrum in microscopic semiconductor crystals. JETP Letters, 40(8), 1136–1139.

García de Arquer, F. P., Talapin, D. V., Klimov, V. I., Arakawa, Y., Bayer, M., & Sargent, E. H. (2021). Semiconductor quantum dots: Technological progress and future challenges. Science, 373(6555), eaaz8541. https://doi.org/10.1126/science.aaz8541.

Hu, J., Li, L., Yang, W., Manna, L., Wang, L., & Alivisatos, A. P. (2001). Linearly polarized emission from colloidal semicouctor quantum rods. Science, 292(5524), 2060–2063. https://doi.org/10.1126/science.1060810.

Ithurria, S., & Dubertret, B. (2008). Quasi-2D colloidal CdSe platelets with thicknesses controlled at the atomic level. Journal of the American Chemical Society, 130(49), 16504–16505. https://doi.org/10.1021/ja807724e.

Kahmann, S., & Loi, M. A. (2020). Trap states in lead chalcogenide colloidal quantum dots—origin, impact, and remedies. Applied Physics Reviews, 7(4), 041305. https://doi.org/10.1063/5.0013166.

Kamat, P. V. (2008). Quantum dot solar cells. Semiconductor nanocrystals as light harvesters. Journal of Physical Chemistry C, 112(48), 18737–18753. https://doi.org/10.1021/jp806791s.

Kayanuma, Y. (1988). Quantum-size effects of interacting electrons and holes in semiconductor microcrystals with spherical shape. Physical Review B, 38(14), 9797–9805. https://doi.org/10.1103/PhysRevB.38.9797.

Loss, D., & DiVincenzo, D. P. (1998). Quantum computation with quantum dots. Physical Review A, 57(1), 120–126. https://doi.org/10.1103/PhysRevA.57.120.

Michalet, X., Pinaud, F. F., Bentolila, L. A., Tsay, J. M., Doose, S., Li, J. J., Sundaresan, G., Wu, A. M., Gambhir, S. S., & Weiss, S. (2005). Quantum dots for live cells, in vivo imaging, and diagnostics. Science, 307(5709), 538–544. https://doi.org/10.1126/science.1104274.

Moreels, I., Lambert, K., Smeets, D., De Muynck, D., Nollet, T., Vanhaecke, F., Vantomme, A., Li, J., Allan, G., & Hens, Z. (2009). Size-dependent optical properties of colloidal PbS quantum dots. ACS Nano, 3(10), 3023–3030. https://doi.org/10.1021/nn900863a.

Munyebvu, N., Lane, E., Grisan, E., & Howes, P. D. (2022). Accelerating colloidal quantum dot innovation with algorithms and automation. Materials Advances, 3(18), 6950–6967. https://doi.org/10.1039/D2MA00139J.

Murray, C. B., Norris, D. J., & Bawendi, M. G. (1993). Synthesis and characterization of nearly monodisperse CdE (E = S, Se, Te) semiconductor nanocrystallites. Journal of the American Chemical Society, 115(19), 8706–8715. https://doi.org/10.1021/ja00072a025.

Nozik, A. J., Beard, M. C., Luther, J. M., Law, M., Ellingson, R. J., & Johnson, J. C. (2010). Semiconductor quantum dots and quantum dot arrays and applications of multiple exciton generation to third-generation photovoltaic solar cells. Chemical Reviews, 110(11), 6873–6890. https://doi.org/10.1021/cr900289f.

Peng, X., Manna, L., Yang, W., Wickham, J., Scher, E., Kadavanich, A., & Alivisatos, A. P. (2000). Shape control of CdSe nanocrystals. Nature, 404(6773), 59–61. https://doi.org/10.1038/35003535.

Resch-Genger, U., Grabolle, M., Cavaliere-Jaricot, S., Nitschke, R., & Nann, T. (2008). Quantum dots versus organic dyes as fluorescent labels. Nature Methods, 5(9), 763–775. https://doi.org/10.1038/nmeth.1248.

Sklénard, B., Mugny, G., Chehaibou, B., Delerue, C., Arnaud, A., & Li, J. (2022). Size and solvation effects on electronic and optical properties of PbS quantum dots. Journal of Physical Chemistry Letters, 13(39), 9044–9050. https://doi.org/10.1021/acs.jpclett.2c02197.

Uwaoma, C. J., Oriaku, C. I., Nwaokorongwu, E. C., & Okwara, E. I. (2025). Theoretical Investigation of Quantum Confinements in Spherical PbSrSe Semiconductor Quantum Dots. Nigerian Journal of Theoretical and Environmental Physics, 3(1), 29–36. https://doi.org/10.62292/njtep.v3i1.2025.60.

Uwaoma, C. J., Oriaku, C. I., Joseph, U., & Nnanna, L. A. (2024). Theoretical Study of Exciton Properties of Dilute GaInAsN Semiconductors. Nigerian Journal of Theoretical and Environmental Physics, 2(2), 194–202. https://doi.org/10.62292/njtep.v2i2.2024.52.

Zhong, X., Feng, Y., Knoll, W., & Han, M. (2003). Alloyed $Zn_xCd_{1-x}S$ nanocrystals with highly narrow luminescence spectral width. Journal of the American Chemical Society, 125(44), 13559–13563. https://doi.org/10.1021/ja0353598.